International Journal of Steel Structures
https://doi.org/10.1007/s13296-024-00873-0

Online ISSN 2093-6311
Print ISSN 1598-2351

A Parametric Investigation on Ultra-low Cycle Fatigue Damage of Steel Bridge Piers Under Horizontal Bi-directional Seismic Excitations

Cheng Cheng[1] · **Xu Xie**[1] · **Mingming Yu**[1]

Received: 4 January 2024 / Accepted: 13 July 2024

Abstract
Ultra-low cycle fatigue (ULCF) damage is one of the main failure modes of steel bridge piers when subjected to severe earthquake. However, existing experimental and numerical studies aiming at ULCF damage of steel piers almost adopt the uniaxial loading strategy, which is different from the real seismic motion. To make up for this problem, the ULCF behavior of steel piers under horizontal bidirectional cyclic loads was investigated in this paper. A two-level zooming analytical system was presented first to save computational cost of the ULCF assessment of steel piers. Its applicability and cost-efficiency were numerically and experimentally verified through detailed elaboration. And based on this, a series of numerical work of piers under horizontal bi-directional and unidirectional cyclic loads were carried out. The relationship between the ductile durability and pier parameters was studied with the help of a micro-damage mechanism-based ULCF assessment method and an energy assumption-based evaluation index. Results showed that compared with the unidirectional loads, bi-directional loads could bring about significant deterioration in the ULCF resistance of piers. The relative ductility capacity of steel piers under bi-directional cyclic loads is approximately consistent as width-to-thickness ratio and slenderness ratio change, and enhances as axial compression ratio increases.

Keywords Ultra-low cycle fatigue · Steel pier · Finite element analysis · Parametric investigation · Bidirectional cyclic loading

1 Introduction

Ultra-low cycle fatigue (ULCF) damage is one of the main failure modes of steel structures under severe earthquakes. During the 1994 Northridge Earthquake in America (Miller, 1998) and the 1995 Kobe Earthquake in Japan (Nakashima et al., 1998), various degrees of ductile fracture were observed at the welded frame connections and the bottom of steel bridge piers. Characterized by ductile cracking, this failure mode is aroused by extremely high strain fluctuations. Local ductile cracks are firstly formed after dozens or even 10 cycles of plastic damage, and further propagate under the subsequent cyclic loads, which leads to the final structural failure. The plastic deformability of steel cannot be fully utilized before the structure fails. Such ductile fracture behavior was replicated in subsequent experimental investigations (Chou & Chen, 2020; Ge et al., 2013; Jia et al., 2015; Li et al., 2022, 2024). So far, researchers have reached consensuses on the cracking behavior and the harmfulness of the ULCF damage.

Great efforts have been devoted to investigating the ULCF assessment methods of steel structures. Based on the micro-mechanism that the ductile fracture is closely related to the local stress triaxiality and plastic strain histories in the damage area (Rice & Tracey, 1969), various evaluation methods have been developed. Typically, these methods can be divided into two categories. The first category is the damage models based on the micro-damage mechanisms, such as the cyclic void growth model (CVGM) developed by Kanvinde et al. (2007), and the continuous damage model (CDM) improved by Tong et al. (2016), which directly take the local stress triaxiality history and the plastic strain history as the computational parameters. Although these methods

✉ Xu Xie
xiexu@zju.edu.cn

Cheng Cheng
11812059@zju.edu.cn

Mingming Yu
12312027@zju.edu.cn

[1] College of Civil Engineering and Architecture, Zhejiang University, Hangzhou 310058, Zhejiang Province, China

Published online: 20 July 2024

are clear in logic, their implementations require very refined solid finite element (FE) analysis, wherein the mesh size in the vulnerable position should be set in accordance with the material characterized length l^* (usually 0.2–0.4 mm) (Kanvinde et al. 2004). This stipulation imposes great computational burden. To reduce the calculation cost, some empirical methods, referred as the second category, were also proposed, including the ULCF assessment method based on the fiber analysis (Yu et al., 2024), the displacement history-based evaluation criteria (Xie et al., 2020) and the modified Coffin-Manson model applied in a wide range of stress triaxiality (Peng et al., 2024). Although these methods do not need the refined solid simulation in the form, their implementation are still based on a large amount of numerical work as the prerequisites, in which the calculation of local stress triaxiality and local plastic strain history are also required. In one word, the acquisition of local stress triaxiality and plastic strain histories based on the refined FE analysis is indispensable for ULCF assessment using current assessment methods.

There are also various numerical investigations on the ULCF properties of steel piers by applying above prediction methods. For instance, Chi (2016) compared the effects of above two types of evaluation methods on elastoplastic analyses of steel piers, and proposed several empirical formulae between the crack initiation life and structural parameters; similar parametric investigations for the influence of the design parameters on the ULCF damage evolution of steel piers were also conducted by Liao (2018) and Tang et al. (2021, 2022) conducted experimental and numerical analysis on the mechanical properties of structural steel under a wide range of pre-fatigue damage, and a set of empirical relationship between the ultimate strength of steel piers and the pre-damage levels was established. However, these studies were all based on the unidirectional cyclic loading protocols. Since the real seismic excitation are complex and multi-directional (Bousias et al., 1996; Wong et al., 1993), applying the ductile behavior regulations derived from these investigations to the practical engineering guidance is unconvincing. What's more, the experimental investigations for the effects of multi-directional load histories on the mechanical behavior of steel piers carried out before by Watanabe et al. (2000) and Goto et al. (2005, 2009) have shown that both the capacity and deformability differ greatly between biaxial response and uniaxial response. Hence, the study of biaxial-properties of ULCF performance for steel piers is of great necessity.

To make up for the problems mentioned above, the ULCF performance of steel piers under lateral biaxial cyclic loads is calculated and discussed, according to an accurate, yet cost-efficient analytical system. In this paper, the research objects are briefly introduced first. Then a two-level zooming analytical system for the ULCF assessment of steel piers was presented. Its efficiency and correctness of the ductility computation was verified numerically and experimentally with sufficient elaboration. Based on this, the ductile performance of the stiffened steel box piers related to the structural parameters was extensively examined by conducting a series of FE analyses, with detailed discussion. The work done in this paper can provide the reference for the seismic design of steel piers in practical engineering.

2 Steel Piers and Loading Protocols

2.1 Steel Piers

The steel pier with stiffened box section were selected as the research object in this paper, whose outline and cross-sectional details are shown in Fig. 1a. To provide an effective engineering guidance, both the material selection and the manufacturing process of steel piers applied in this paper refer to the practical engineering application: (1) Piers are made of Q345qC steel, which is a commonly used material in Chinese steel bridges; (2) Full penetrating welding process is adopted for the connection of stiffening plates and end plates. And the detailed welding process flow is presented in Fig. 1b, by which the distribution of base material and weld material is identified. The main structural parameters of steel piers include the slenderness ratio λ_B, the width-to-thickness ratio R_R, the axial compression ratio P/P_y and the relative stiffness of stiffeners. The calculation of λ_B and R_R are formulated as (Ge et al., 2013; Zhuge et al., 2020):

$$\lambda_B = \frac{2h}{r}\frac{1}{\pi}\sqrt{\frac{\sigma_y}{E}} \tag{1}$$

$$R_R = \frac{B}{t}\sqrt{\frac{12\left(1-\nu^2\right)}{4\pi^2 n_r^2}}\sqrt{\frac{\sigma_y}{E}} \tag{2}$$

where h is the height of piers; r denotes the radius of rotation in deformed direction; B is the width of flange; t is the thickness of stiffening plate; n_r is the number of regions divided by stiffeners in stiffening plate; $\nu = 0.3$, is the Poisson's ratio. Stipulated by the design code (Ministry of Transport of the People's Republic of China, 2015), the stiffener's relative stiffness is defined and limited as follows:

$$\frac{b_s}{t_s} \leqslant 12\sqrt{\frac{345}{\sigma_y}} \tag{3}$$

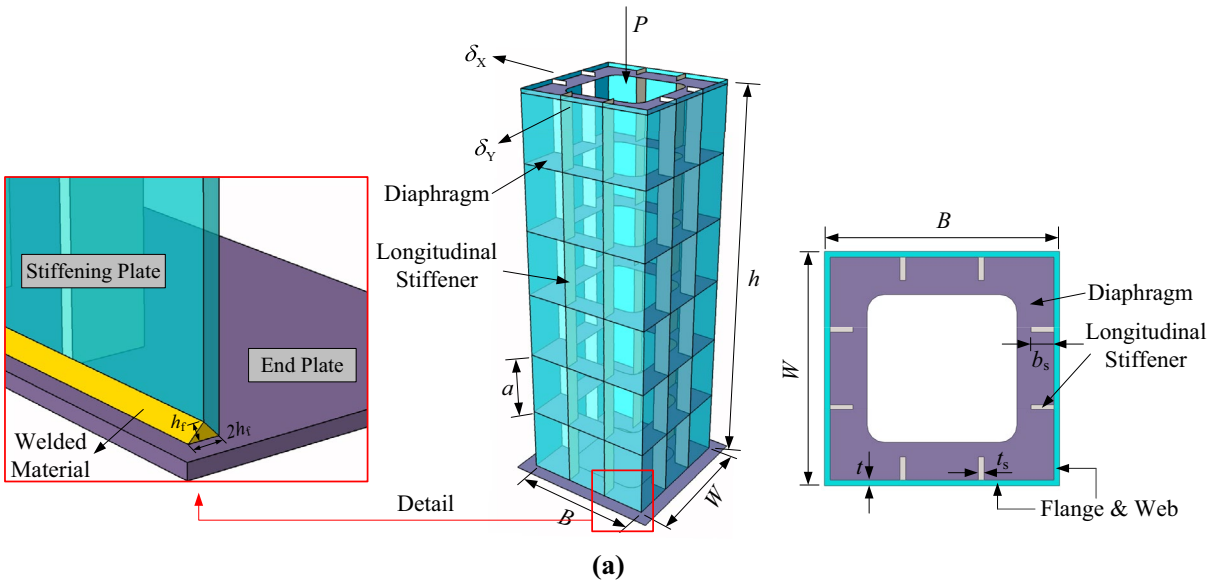

(a)

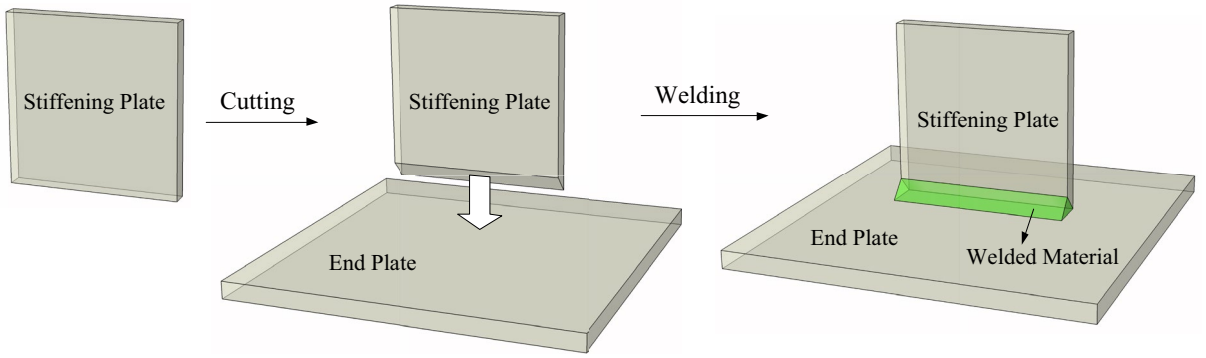

(b)

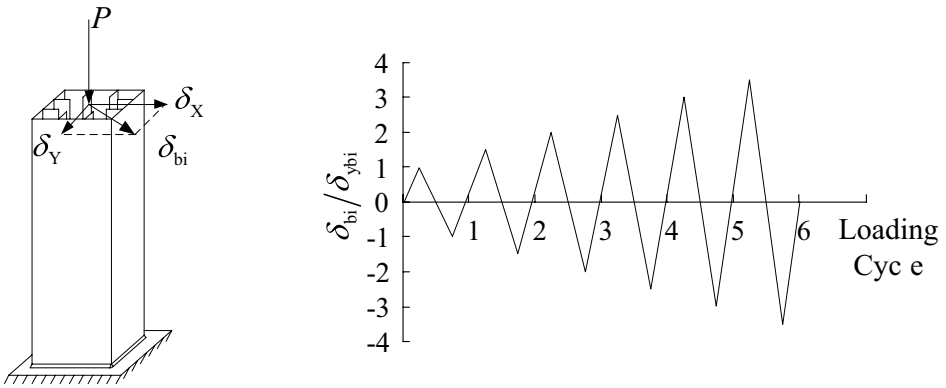

(c)

Fig. 1 Stiffened box steel pier structure and cyclic load pattern **a** structural form; **b** Full penetrating welding process; **c** C1 protocol

$$\begin{cases} \dfrac{\gamma}{\gamma^*}=\dfrac{EI_l}{BD'\gamma^*} \geqslant 1 \\ \gamma_t=\dfrac{EI_t}{BD'} \geqslant \dfrac{1+n_r\gamma}{4(a/B)^3} \end{cases} \tag{4}$$

$$\gamma^*=\begin{cases} \frac{1}{n_r}\left[4{n_r}^2\left(1+n_r\frac{b_s t_s}{Bt}\right)\alpha^2-\left(\alpha^2+1\right)^2\right] & \alpha \leqslant \sqrt[4]{1+n_r\gamma} \\ \frac{1}{n_r}\left\{\left[2{n_r}^2\left(1+n_r\frac{b_s t_s}{Bt}\right)\alpha^2-1\right]^2-1\right\} & \alpha > \sqrt[4]{1+n_r\gamma} \end{cases} \tag{5}$$

where γ and γ_t denote the relative stiffness of longitudinal stiffeners and diaphragms respectively; I_l and I_t are bending moment of inertia of a single longitudinal stiffener and a single diaphragm, respectively; D' is the bending stiffness of steel plates per unit width; a is the spacing of transverse partitions; t_s and b_s are the thickness and width of vertical stiffener respectively; γ^* represents the optimal stiffness ratio of stiffeners, which is defined by Eq. (5); $\alpha=a/B$, is the spacing ratio of the diaphragm.

In past investigations (Goto et al., 2005, 2009; Watanabe et al., 2000), it was found that the mechanical properties of steel piers, such as the overall stiffness evolution, the critical capacity and the energy dissipation ability are closely related to the slenderness ratio λ_B, the width-to-thickness ratio R_R and the axial compression ratio P/P_y. Thus, these three structural parameters were applied in this paper to investigate its effect on the ULCF performance of steel piers under horizontal bi-directional cyclic loads. Catering to the practical engineering, λ_B was determined in the range of 0.20–0.50; R_R was determined in the range of 0.25–0.45; and P/P_y ranged from 0.10 to 0.30. Based on these, 16 steel piers were designed, in which 4 piers were loaded unidirectionally, termed with "UN", and 12 piers were loaded bi-directionally, termed with "BI". Table 1 exhibits the geometric dimensions and design parameters of these piers. In terms of the naming format of different pier structures Sxx-xxPxx, S indicates steel pier, and the subsequent three numbers represent the slenderness ratio, width-to-thickness ratio and axial compression ratio, respectively. Taking pier S20-30P15 as an example, it is indicated λ_B equals to 0.20, R_R equals to 0.30 and P/P_y equals to 0.15.

2.2 Bidirectional Cyclic Loading Protocols

The biaxial load is the combination of a vertical constant pressure P and lateral cyclic displacements δ_X and δ_Y applied at the top of piers, representing the dead load transmitted from the superstructure and the seismic loads, respectively. As for the unidirectional loading process, there is only δ_X for lateral cyclic displacement. According to the experimental conclusions of steel piers studied by Watanabe et al. (2000), the biaxial-linear loading path at 45° along the sectional spindle, which is the most vulnerable condition of bi-directional cyclic loading patterns, was adopted in this paper. The oblique displacement δ_{bi} is formed as:

$$\delta_{bi}=\sqrt{\delta_X^2+\delta_Y^2} \tag{6}$$

where δ_X and δ_Y are the decomposed displacements along the two sectional axes respectively. As shown in Fig. 1c, the C1 protocol, with 0.5 times of δ_{ybi} as the cyclic displacement increment per cycle, was utilized. The δ_{ybi} represents the yield displacement along the 45° direction of the main axis, and there is a simple conversion relationship: $\delta_{ybi}=1/\sqrt{2}\cdot\delta_{x0}$. Suggested by Ge et al. (2013), the yield displacement

Table 1 Geometrics of designed piers

Loading type	No.	h/m	B/m	W/B	n_r	t/m	t_s/m	b_s/m	a/m
BI	S20-25P15	2.50	0.825	1.0	3	0.024	0.024	0.076	0.4125
	S20-30P10	2.50	0.825	1.0	3	0.020	0.020	0.067	0.4125
	S20-30P15	2.50	0.825	1.0	3	0.020	0.020	0.067	0.4125
	S20-30P20	2.50	0.825	1.0	3	0.020	0.020	0.067	0.4125
	S20-30P25	2.50	0.825	1.0	3	0.020	0.020	0.067	0.4125
	S20-30P30	2.50	0.825	1.0	3	0.020	0.020	0.067	0.4125
	S20-35P15	2.50	0.825	1.0	3	0.017	0.017	0.060	0.4125
	S20-40P15	2.50	0.825	1.0	3	0.015	0.015	0.055	0.4125
	S20-45P15	2.50	0.825	1.0	3	0.013	0.013	0.050	0.4125
	S30-30P15	3.75	0.825	1.0	3	0.020	0.020	0.067	0.4125
	S40-30P15	5.00	0.825	1.0	3	0.020	0.020	0.067	0.4125
	S50-30P15	6.25	0.825	1.0	3	0.020	0.020	0.067	0.4125
UN	S20-30P10	2.50	0.825	1.0	3	0.020	0.020	0.067	0.4125
	S20-30P15	2.50	0.825	1.0	3	0.020	0.020	0.067	0.4125
	S20-35P15	2.50	0.825	1.0	3	0.017	0.017	0.060	0.4125
	S30-30P15	3.75	0.825	1.0	3	0.020	0.020	0.067	0.4125

δ_{x0} of steel box columns along the main sectional axes is the composition of the bending yield displacement δ_{B0} and the shear yield displacement δ_{S0}, which is formulated as:

$$\delta_{x0} = \delta_{B0} + \delta_{S0} = \frac{H_{x0}h^3}{3EI} + \frac{H_{x0}h}{\kappa GA} \tag{7}$$

$$\begin{cases} H_{x0} = \dfrac{M_y}{h}\left(1 - \dfrac{P}{P_y}\right) \\ H_{x0} = \dfrac{M_y}{0.85h}\left(1 - \dfrac{P}{P_E}\right)\left(1 - \dfrac{P}{P_u}\right) \end{cases} \tag{8}$$

where I is the moment of inertia; κ is the shear nonuniformity coefficient of the section, taken as 5/6; G is the shear modulus; H_{x0} denotes the uniaxial yield thrust, determined by the smaller value of Eq. (8); M_y is the yield moment; P_E, P_u and P_y represent Euler's buckling load, the ultimate strength and the yield axial force, respectively.

3 FE Models

3.1 Analytical System

Given the severe difference between the characteristic length l^* of the metal and the macro size of piers, the two-level zooming strategy based on the sub-model technique was advised in this paper to overcome the great computational burden imposed by the ULCF assessment. As illustrated in Fig. 2a, the first level zooming is constituted of the global model and the sub1 model; the second level zooming is constituted of the sub1 model and the sub2 model. The whole analytical system was implemented on the commercial FE platform ABAQUS.

The global model includes the whole content of the pier, in which a small range at the top is modelled by beam element to transfer the loads, and the rest is modelled by four-node thick shell element (referred as S4R) to reflect the potential local buckling behavior of the steel plates. The welding details are ignored in the global model. The followed sub1 model represents a part of the pier bottom, entirely modeled by eight-node reduced integration solid element (referred as C3D8R). In this model, the geometry of weld is reflected, meshed with a mesh size rougher than l^*. To cater to the change of bending stress along the thickness direction of the plates, at least 4 layers of solid elements are suggested (Shi & Zhou, 2006). The final sub2 model is used to simulate the weld, and its mesh size is controlled at 0.2 mm, corresponding to the l^* of Q345qC steel (Liao, 2018). According to the Saint–Venant principle, the exposed surfaces of each sub-model are kept at least 1.5 times the width or thickness away from the calculated area to ensure the reliability of the strain and stress solution of the area of interest, such as 1.5B or 1.5t. The Chaboche hybrid hardening model is applied to accurately express the cyclic metal plasticity. And the constitutive constants of Q345qC steel and its weld material refer to our previous study (Liao, 2018). As for the operation of these three models, the sub1 model applies the interpolated nodal displacement solution of the global model as the displacement controls on its exposed boundaries. Similarly, the sub2 model is driven by the processed results of sub1 calculations.

A typical micro-damage mechanism based ULCF damage assessment model, the CVGM (Kanvinde et al., 2007), was applied to give a reference of the ductility judgement of steel piers. This model has two main issues: the nonnegative cyclic void growth index VGI_{cyclic} and the cyclic void capacity index $VGI_{\text{cyclic}}^{\text{critical}}$, which are formulated as:

$$VGI_{\text{cyclic}} = \sum_{\text{tensile}} \int_{\varepsilon_1}^{\varepsilon_2} \exp(|1.5T|)\mathrm{d}\varepsilon_p - \sum_{\text{compressive}} \int_{\varepsilon_1}^{\varepsilon_2} \exp(|1.5T|)\mathrm{d}\varepsilon_p \geqslant 0 \tag{9}$$

$$VGI_{\text{cyclic}}^{\text{critical}} = \eta \cdot \exp\left(-\lambda \varepsilon_p^{\text{accumulated}}\right) \tag{10}$$

where the upper and lower limits of the integral in Eq. (9), ε_1 and ε_2, represent the equivalent plastic strain at the start and end of each tensile cycle and compressive cycle, respectively; T represents the stress triaxiality, derived by the ratio of hydrostatic pressure σ_m and mises stress σ_{eq}; $\mathrm{d}\varepsilon_p = \sqrt{(2/3)d\varepsilon_{ij}^p d\varepsilon_{ij}^p}$, signifies the incremental equivalent plastic strain; η and λ symbolize the initial ductility capacity and damage degradation constants, separately; $\varepsilon_p^{\text{accumulated}}$ is the cumulative equivalent plastic strain at the start of each tensile cycle. It is assumed that ULCF fracture occurs when $DI = VGI_{\text{cyclic}} \Big/ VGI_{\text{cyclic}}^{\text{critical}} \geqslant 1$. According to our previous study (Xie et al., 2020), these two constants of Q345qC steel were taken as $\eta = 2.03$ and $\lambda = 0.10$ in this paper.

3.2 Numerical Verification

The numerical verification involves the comparison between the simulated results derived from the two-level zooming analytical system and the conventional FE modeling. For the convenience of the FE computation of the conventional modeling, a scaled steel pier was applied here, with pier height of 0.25 m, flange width of 0.08 m, stiffening plate thickness of 0.002 m, stiffer thickness of 0.002 m and stiffener width of 0.01 m. This pier was loaded under the C1 protocol depicted in Fig. 1c. The FE model established based on the hybrid FE modeling

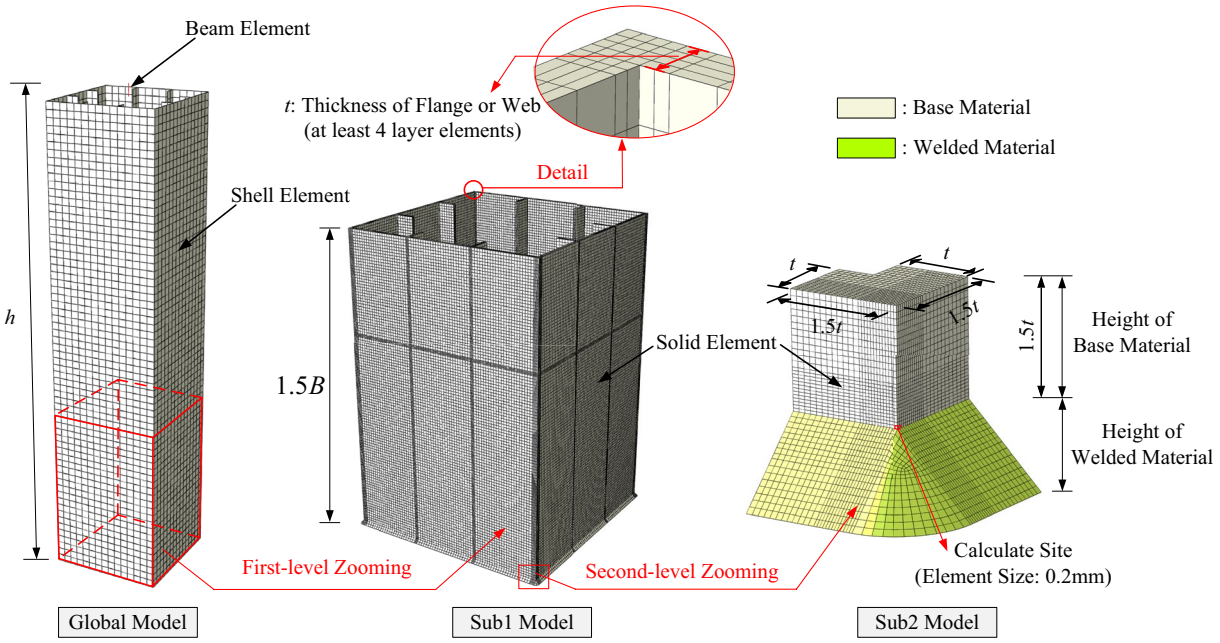

(a)

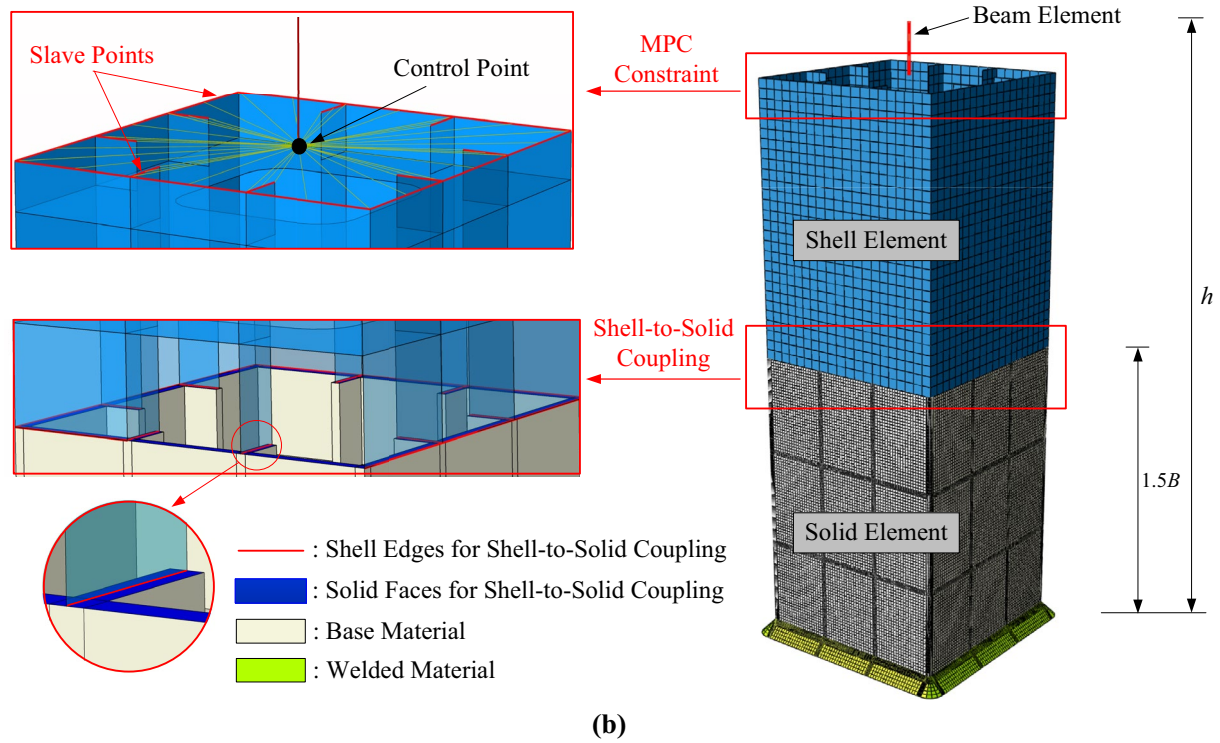

(b)

Fig. 2 FE models **a** two-level zooming analytical system; **b** Hybrid FE model

strategy, which is a commonly used method applied in recent researches (Tang et al., 2021; Wang et al., 2018; Xie et al., 2018), was adopted as a numerical comparison, as shown in Fig. 2b. Very refined mesh size, corresponding to the material characterized length l^*, is locally partitioned in the four corners. Displacements between beam elements and shell elements are coordinated by MPC coupling, and the shell-to-solid coupling is used for the connection of shell elements and solid elements.

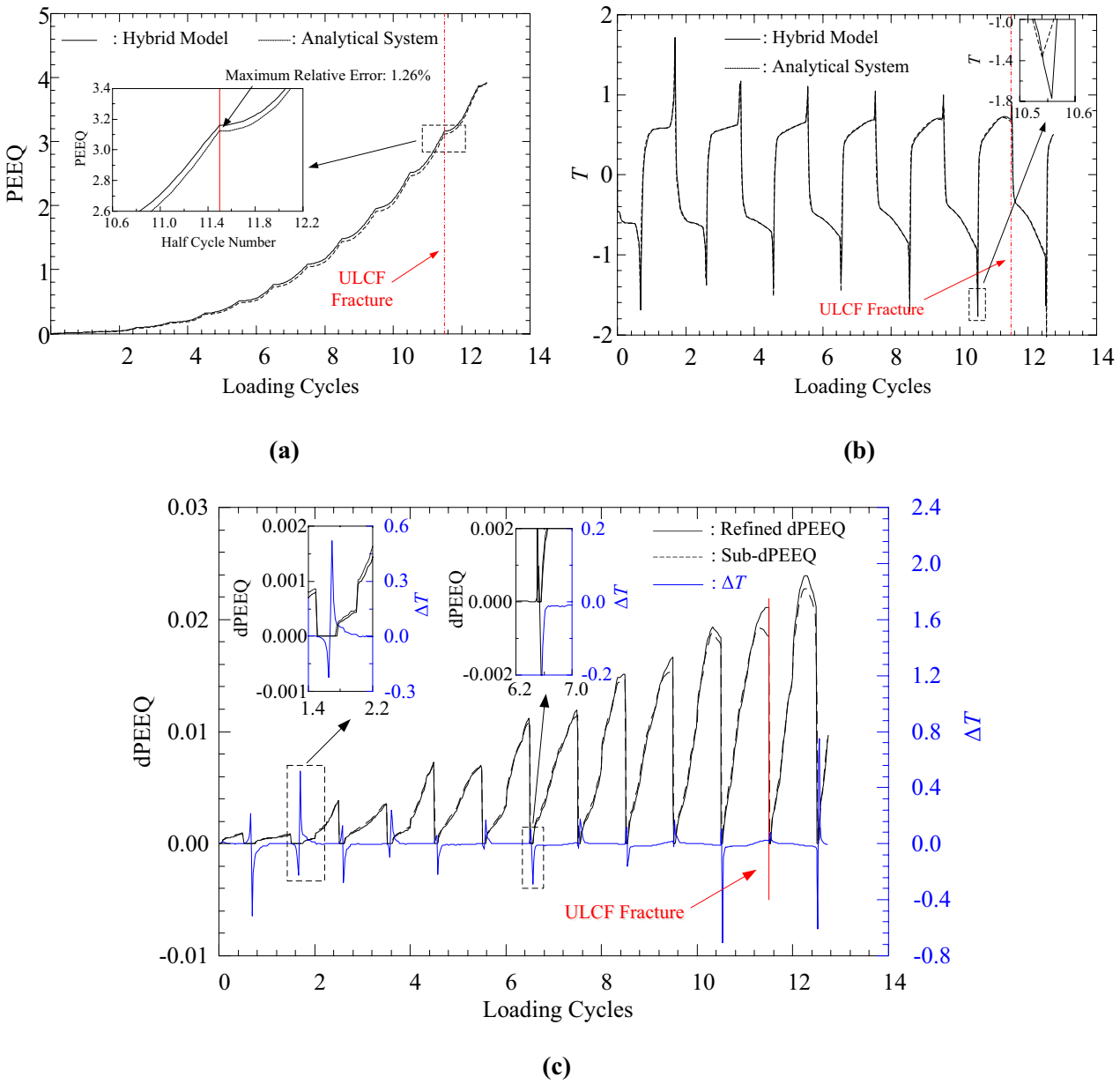

Fig. 3 Numerical comparisons **a** PEEQ history; **b** *T* history; **c** Comparisons of PEEQ and T in an identical coordinate system

The numerical comparison is summarized in Fig. 3, including the cumulative plastic strain (PEEQ) history and stress triaxiality (*T*) history. The comparison of PEEQ histories shown in Fig. 3a suggests a gradually increased error as the load progresses. The maximum error is 1.26%, which is of an acceptable range. Comparisons in Fig. 3b suggest a good correlation between stress histories, except some sections where stress changes rapidly. In these sections, the relative error can be up to 40%, which is far beyond the trusted range. Noticing that the existing ULCF assessment method are all implemented based on the integration of the stress triaxiality on the PEEQ increment, attempts were made to plot these two types of data in an identical coordinate system to make a better judgement of the huge errors, which is shown in Fig. 3c. The dPEEQ means the cumulative plastic strain increment between adjacent computational steps, and ΔT denotes the absolute error of *T* of the two types of numerical analyses. As plotted, the plastic strain increment is almost zero for all sections with large error of *T*. Thus, such huge errors do little to the ULCF damage evaluation under this condition. Besides, it is common that the step increment for nonlinear FE analysis varies greatly as the calculation condition changes. In sections where the stress changes rapidly, even a small alternation in time step can bring about a huge change in the display of results. The great

Table 2 Comparison of computational costs

Items	Hybrid FE models	Two-level zooming models
Total number of elements	458,013	8170 + 180,760 + 14,598
Time of analysis	3292 (min)	6 + 362 + 21 = 389 (min)
Solution data file size	54.3 GB	0.9 + 24.5 + 1.6 = 27.0 GB
Physical memory usage	39.5 GB	15.6 GB

error shown in Fig. 3b may not exist. Further still, the fracture initiations N_{fn} obtained by CVGM are 11.46 cycles and 11.48 cycles for the hybrid FE models and the two-level analytical system, respectively. They are very close to each other. The computational costs listed in Table 2 also gives the evidence to the great cost-efficiency brought by the two-level zooming analytical system.

3.3 Experimental Verification

The application of the analytical system was also verified experimentally. In our previous studies of the seismic performance of steel pier (Li et al., 2022), two steel pier specimens, SP-A and SP-B were tested. Table 3 lists the geometrics of these two piers. Pier specimens were fixed between the top beam and the foundation by high-strength bolts. The enforced cyclic displacement was along the 45° direction of the sectional main axis. The loading protocol was C1 loading protocol, as shown in Fig. 1c.

Figure 4a shows the hysteresis curves comparison between the FE analysis and test. It can be observed that some pivotal properties, such as the structural stiffness revolution, peak capacity, and skeleton curve shape, keep good consistency between the two. The ULCF initiations derived from the tests and numerical work are listed in Table 3, termed as N_{ft} and N_{fn}, respectively. And there are only slight errors between them. The damage evolutions for the most critical element of the two pier specimens are presented in Fig. 4b and c shows the equivalent plastic strain nephogram near the weld toe and the ULCF cracks observed in the test. It can be found that the plastic strain is highly concentrated at the corner element, and the ductile cracks also initiated at this vulnerable site, providing the evidence for the reliability of ULCF assessment of the analytical system.

From the numerical and experimental verification discussed above, it can be concluded that the presented two-level zooming analytical system is feasible and convenient for the ULCF analysis of steel piers.

4 Parametric Investigation

Following the modeling procedures of the two-level zooming analytical system, all 16 steel piers designed in Table 1 were analyzed. Their ductile fracture assessment results are summarized in Table 4. Besides, nonlinear dynamic analyses were carried out on piers S20-30P10, S20-30P15, S20-35P15 and S30-30P15 with unidirectional and bidirectional seismic wave inputs, respectively. The selected seismic wave is the Northridge earthquake recorded by the LDM station in 1994, which is one of the representative examples of near-field seismic motion. Its acceleration time histories in the east–west (EW) and north–south (NS) directions are shown in Fig. 5a. And Fig. 5b–e present the ULCF damage evolution of the four piers. It is apparent that there is a huge discrepancy of the ULCF damage initiations under unidirectional cyclic loads and bidirectional cyclic loads. This attests that in comparison with unidirectional loading patterns, not only the hysteretic behaviors (Goto et al., 2005, 2009; Watanabe et al., 2000), but also the ductility capacity has a significant deterioration for piers loaded bi-directionally. The necessity of the investigation on ULCF performance under such vulnerable loading conditions is further indicated.

As illustrated in Fig. 1c, the applied cyclic loading protocol is controlled by yield displacement of each pier member. Under this controlling pattern, the equality of the plastic deterioration degree for different structures can be ensured. Only in this way can the comparison between different structural members be feasible. Generally, although the ULCF initiation life calculated by CVGM does reflect the ductility resistance to a certain extent, the discrepancy in load histories cannot be included. In other words, N_{fn} is only suitable and meaningful for ULCF evaluation and comparison under the same

Table 3 Geometrics of pier specimens

No.	h/m	B/m	W/B	h_f/mm	n_r	t/mm	t_s/mm	b_s/mm	a/m	N_{ft}	N_{fn}
SP-A	1.25	0.32	1.0	7.4	3	7.4	7.4	39	0.16	7	8
SP-B	0.65	0.20	1.0	7.4	2	7.4	7.4	34	0.10	7	7

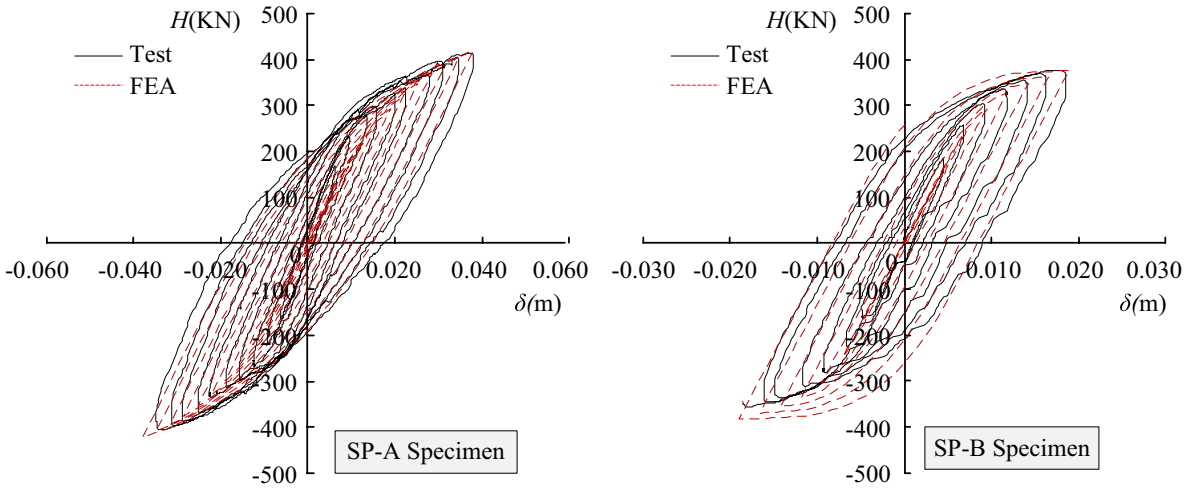

(a)

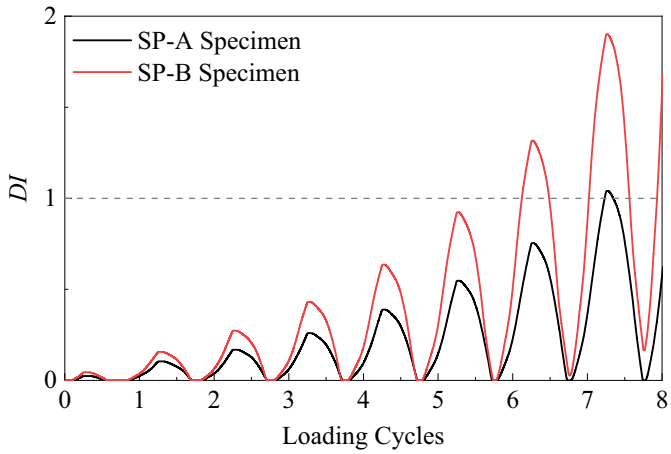

(b)

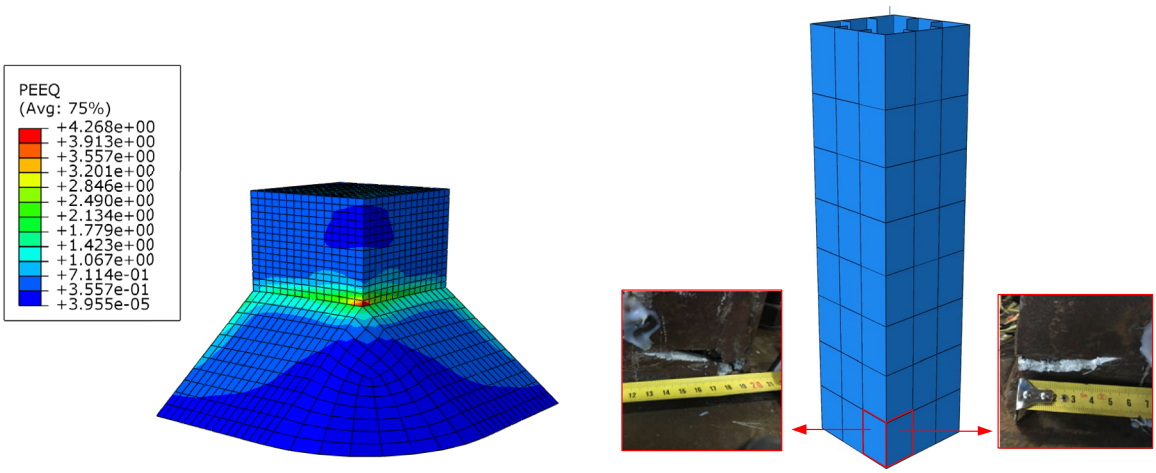

(c)

Fig. 4 Experimental verification of steel piers **a** hysteresis curves comparison; **b** Damage evolution at the weld corner; **c** PEEQ nephogram and cracking behavior of the weld corner

Table 4 Results of ULCF fracture initiations (unit: half cycle)

Loading type	No.	N_{fn}
BI	S20-25P15	10.76
	S20-30P10	7.75
	S20-30P15	10.74
	S20-30P20	12.79
	S20-30P25	12.79
	S20-30P30	18.88
	S20-35P15	9.80
	S20-40P15	9.74
	S20-45P15	9.76
	S30-30P15	8.76
	S40-30P15	7.78
	S50-30P15	7.71
UN	S20-30P10	69.78
	S20-30P15	88.62
	S20-35P15	85.74
	S30-30P15	81.76

working condition. However, due to the loading differences between different pier members, the ULCF life N_{fn} cannot be applied as the direct judgement for the parametric comparison. Given that, the comparison of the ductile capacity of different piers was conducted by applying an energy dissipation-based evaluation index D_E as a supplement in this paper, which is determined by the ratio of totally absorbed energy to the elastic energy stored. The total energy consumption is calculated by the area enclosed by the load-displacement hysteretic curve from the load beginning to the final ductile cracking. While the stored elastic energy is computed by the area enclosed by the monotonically loaded load-displacement curve from the beginning to the yield, regarded as a mechanical characteristic of the structure. It is deemed that the larger the value of D_E, the stronger the ductility resistance of the structure. This nondimensional energy dissipation-based evaluation index eliminates the influence of the loading discrepancy, providing a more projective measure for the response of ULCF performance. Based on this, detailed parametric discussions of biaxial-ULCF behavior are presented below.

4.1 Effects of Width-to-Thickness Ratio R_R

The analyses of series S20-R_RP15-BI piers reflect the influence of parameter R_R on ULCF performance of piers under horizontal bi-directional cyclic loads. From Fig. 6a, it is observed that the fatigue initiation life decreases slightly with the increase of R_R, except for the pier S20-45P15-BI. For the PEEQ history regulation, this abnormal fluctuation also appears in the pier S20-45P15-BI, as plotted in Fig. 6b. The continued decline existing in initial cracking lives with the increase of R_R is of an intelligible mechanic law, while the fluctuation occurred in pier S20-45P15-BI is an abnormality. To have a reasonable illustration, comparison was made for the plate deformation of these five piers at the instant of ULCF initiation, as shown in Fig. 6d. It is found that under the same loading amplitude, the local buckling damage is prone to occur in steel plates with the increase of R_R. And this is especially prominent for the pier S20-45P15-BI. The decrease of plastic damage concentrated at the weld joint of pier S20-45P15-BI may be caused by the shared plastic deformability generated from the plates' local buckling, and this prolongs the fatigue initiation life.

A further insight into the effect of the variation of plate thickness is obtained by the energy dissipation-based index D_E, which is presented in Fig. 6c. Results suggest that although a certain pattern between the initial cracking life N_{fn} and width-to-thickness ratio R_R is observed, the energy dissipation ability from initial loading to final fracture fluctuates within a quite small range. More specifically, the change of plate thickness contributes little to the relative ULCF resistance improvement of piers.

4.2 Effects of Slenderness Ratio λ_B

The analyses of series Sλ_B-30P15-BI piers reflect the influence of parameter λ_B on ULCF performance of piers under horizontal biaxial cyclic loads. The trend exhibited in Fig. 7a indicates a processive decrease of ULCF life N_{fn} with the increase of λ_B, and this is also proved by the comparisons of PEEQ histories depicted in Fig. 7b. Attention should be paid that in the parametric study of ULCF behavior of steel piers under unidirectional cyclic loads carried out by Chi (2016), conclusion was drawn that the fracture initiation life is substantially retained as λ_B changes. While in another parametric investigation, which was also under the unidirectional cyclic loading conditions, Liao (2018) found that the fatigue initiation life increases with the enhancement of λ_B. All of these are quite different from the regulation obtained in Fig. 7a. On the one hand, it is noted that the parameter λ_B, which represents the slenderness of piers, is merely defined based on the pier geometrics. One of the computational factors in Eq. (1), the r, is computed along the sectional spindle only. The calculated parameter r varies scarcely for the unidirectional and bidirectional loaded piers. The description of pier slenderness is confusing when subjected to complex loads such as biaxial-circular form. Thus, potential reasons for these huge discrepancies may be the blurred description of piers' slenderness. The relation between loads and pier slenderness needs a further modification. On the other hand, in the parametric investigation of parameter λ_B, lateral loads vary greatly from each other as the height of pier changes according to Eqs. (7–8). The ULCF life N_{fn}, which is expressed in the number of loading cycles, cannot take

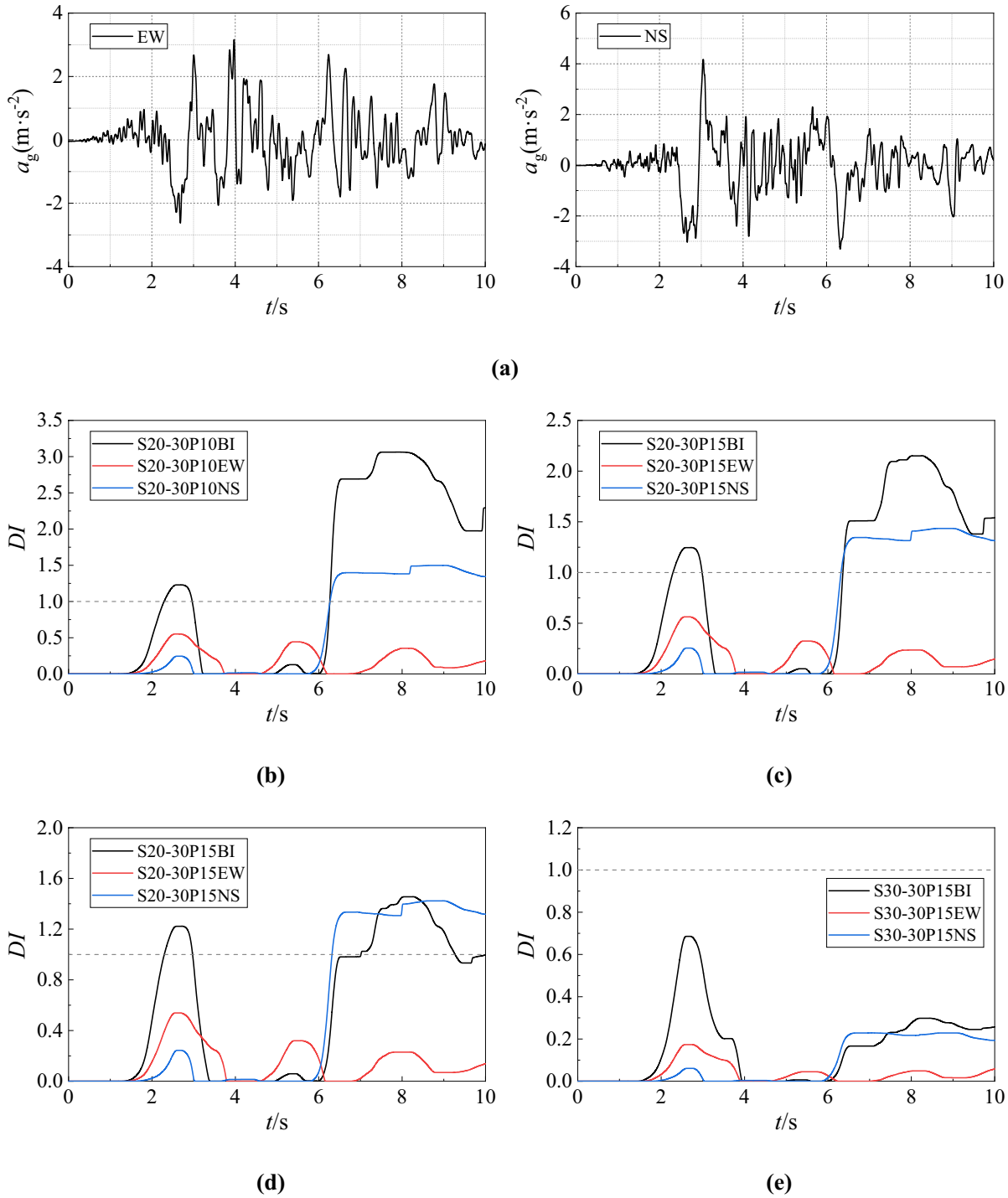

Fig. 5 Comparation of pier ULCF damage evolution under unidirectional and bidirectional seismic excitations **a** horizontal bidirectional acceleration time history; **b** Damage evolution of S20-30P10; **c** Damage evolution of S20-30P15; **d** Damage evolution of S20-35P15; **e** Damage evolution of S30-30P15

into account the load discrepancies. Standard is lost when using N_{fn} for the analysis of parameter λ_B.

As plotted in Fig. 7c, the relation of the ULCF property and slenderness ratio λ_B is further explained by the dimensionless index D_E. Noticing the yield displacement-based loading protocol, it can be safely concluded that within the same plastic degradation degree, the relative ULCF resistance of piers with various λ_B is approximately consistent. In practical engineering, undergoing the same seismic excitation, a higher bridge pier design is suggested to

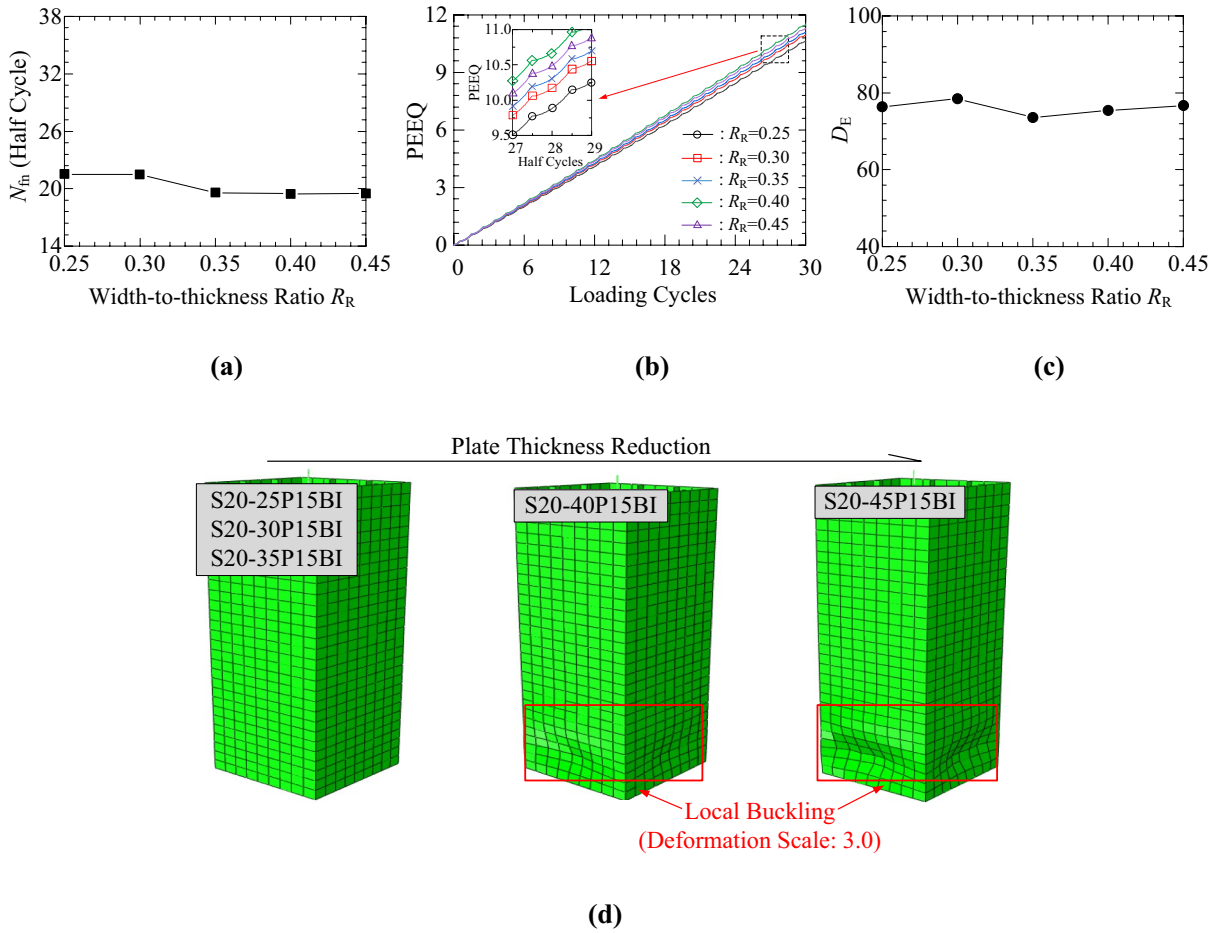

Fig. 6 Effects of parameter R_R **a** comparison of ULCF life; **b** Comparison of PEEQ; **c** Comparison of index D_E; **d** Comparison of plate deformation

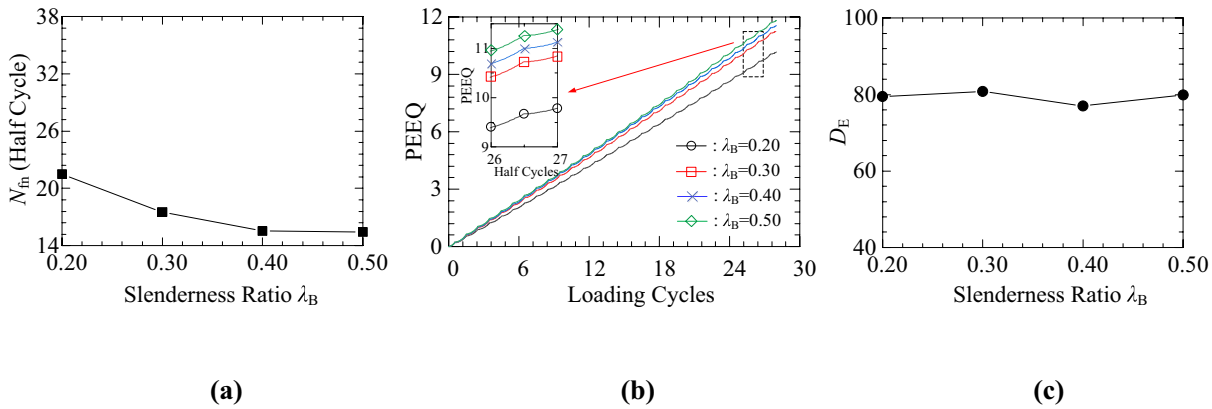

Fig. 7 Effects of parameter λ_B **a** comparison of ULCF life; **b** Comparison of PEEQ; **c** Comparison of index D_E

have a stronger ULCF resistance. This is further supported by the observed differences in damage evolution between piers S20-30P15 and S30-30P15 under seismic excitations (Fig. 5).

4.3 Effects of Axial Compression Ratio P/P_y

The analyses of series S20-30P/P_y-BI piers reflect the influence of parameter P/P_y on ULCF performance of piers under

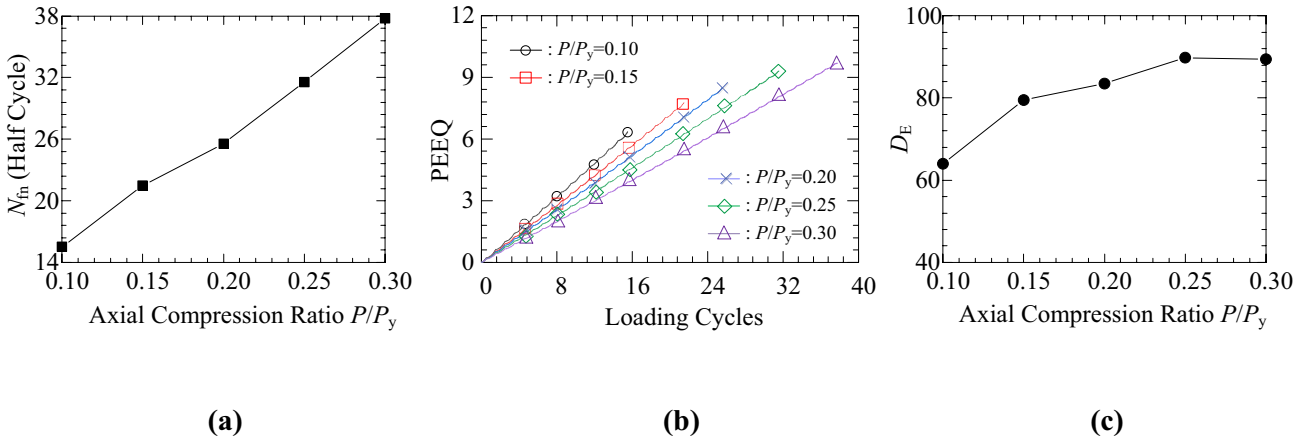

Fig. 8 Effects of parameter P/P_y **a** Comparison of ULCF life; **b** Comparison of PEEQ; **c** Comparison of index D_E

horizontal biaxial cyclic loads. Results in Fig. 8a show an obvious enhancement of N_{fn} as P/P_y increase, and this variation is also implied by the PEEQ histories plotted in Fig. 8b. Similar conclusions were also admitted in parametric studies under unidirectional cyclic loads carried out by Chi (2016) and Liao (2018). Besides, indicated by Fig. 8c, for piers under the same plastic degeneration cycles, a higher P/P_y would bring about a stronger relative energy absorbability. The huge discrepancy lies in the comparison of different P/P_y is in sharp contrast to the roughly consistency indicated by the above two parametric discussions, which suggests that the relative ductility resistance of steel piers is more susceptible to axial comparison ratio P/P_y.

There are two possible reasons that contribute to the regulations derived above. On the one hand, according to Eqs. (7–8), the increase of P/P_y would cause a great reduction of the lateral displacement amplitudes. Under the yield displacement-based loading patterns, the decreased lateral loading amplitude weakens the plastic damage concentrated at weld joints, which further affects the ULCF performance. On the other hand, from the perspective of micro-damage mechanism, the increased pressure may inhibit the growth of the micro void at welded joints, and then strengthens its ULCF resistance, which can be used to illustrate the increase of the relative ductility shown in Fig. 8c.

5 Conclusion

In this paper, an effective ULCF simulation system for ULCF computation of steel piers was presented, and the verification of its reality and correctness were also performed numerically and experimentally. And based on this, a series of analytical work for ULCF performance of steel bridge piers were conducted, by which the discrepancy between uniaxial and biaxial ULCF behaviors, as well as the parametric properties of biaxial-ductility were investigated. The main conclusions are summarized as follows:

1. In comparison with the commonly applied hybrid FE modeling method, the presented two-level zooming analytical system can significantly reduce the computational cost while maintaining the results' accuracy; and the error between experimental and numerical results is also acceptable.
2. Compared with pier members loaded unidirectionally, bi-directional cyclic loading pattern can lead to severer deterioration of the ULCF performance.
3. Under bi-directional cyclic loads, the relative ductility capacity of steel piers is approximately consistent as width-to-thickness ratio R_R and slenderness ratio λ_B vary, and enhances as axial compression ratio P/P_y increases. Among them, the ULCF performance of piers under bidirectional cyclic loads is more sensitive to parameter P/P_y.
4. Within the same degree of plastic damage, the local buckling is prone to occur at stiffening plates in a thinner pier, as other parameters remain unchanged. The plastic deformability produced by the local buckling could share the plastic degeneration accumulated at welded joints, which further prolongs the ULCF life. But the relative energy dissipation ability remains unchanged.
5. In contrast with other structural parameters of steel piers, it is found that the parametric regulations between ULCF capacity and the parameter slenderness ratio λ_B are more susceptible to loading dimensions. The influence of different loading modes on parameter λ_B needs further work.

Acknowledgements The study described in this paper was supported by the grant from the Natural Science Foundations of China (52178174 and 51878606). Besides, further appreciation is given to Dassault Systèmes Simulia Corporation for the FE simulation of the powerful commercial FE software ABAQUS-6.14.

References

Bousias, S. N., Verzeletti, G., Fardis, M. N., & Gutierrez, E. (1996). Load-path effects in column biaxial bending with axial force. *Journal of Engineering Mechanics, 121*(5), 596–605.

Chi, S. (2016). *Predicting extremely low-cycle fatigue cracking initiation life of steel bridge piers*. Master's Thesis, Shanghai Jiaotong University, Shanghai, China. (In Chinese).

Chou, C., & Chen, G. (2020). Lateral cyclic testing and backbone curve development of high-strength steel built-up box columns under axial compression. *Engineering Structures*. https://doi.org/10.1016/j.engstruct.2020.111147

Ge, H., Kang, L., & Tsumura, Y. (2013). Extremely low-cycle fatigue tests of thick-walled steel bridge piers. *Journal of Bridge Engineering, 18*(9), 858–870.

Goto, Y., Jiang, K., & Obata, M. (2005). Hysteretic behavior of thin-walled circular steel columns under cyclic biaxial loading. *Journal of Structural Engineering and Earthquake Engineering, 780*, 181–198.

Goto, Y., Muraki, M., & Ebisawa, T. (2009). Ultimate state and design of thin-walled circular steel columns under bi-directional seismic excitations. *Journal of Structural Engineering, 55A*, 629–642.

Jia, L., Ge, H., Suzuki, T., & Luo, X. (2015). Experimental study on cracking of thick-walled beam-column connections with incomplete penetration in steel bridge piers. *Journal of Bridge Engineering, 20*(4), 1–13.

Kanvinde, A. M. (2004). *Micromechanical simulation of earthquake-induced fracture in steel structures*. Doctoral Thesis, Stanford University, Palo Alto.

Kanvinde, A. M., Deierlein, G. G., Kanvinde, A. M., & Deierlein, G. G. (2007). Cyclic void growth model to assess ductile fracture initiation in structural steels due to ultra low cycle fatigue. *Journal of Engineering Mechanics, 133*(6), 701–712.

Li, S., Lin, J., Zhuge, H., Xie, X., & Cheng, C. (2022). Ultra-low cycle fatigue fracture initiation life evaluation of thick-walled steel bridge piers with microscopic damage index under bidirectional cyclic loading. *Structures*. https://doi.org/10.1016/j.istruc.2022.06.026

Li, Y., Li, H., & Wang, X. (2024). Ultra-low cycle fatigue test study of bolted spherical joints in steel grid structures. *Materials*. https://doi.org/10.1016/j.istruc.2024.106222

Liao, Y. (2018). *Research on ultra low cycle fatigue properties and fracture mechanism of steel bridge welded joint*. Master's Thesis, Zhejiang University, Hangzhou, China. (In Chinese).

Miller, D. K. (1998). Lessons learned from the Northridge earthquake. *Engineering Structures*, *20*(4–6), 249–260.

Ministry of Transport of the People's Republic of China. (2015). *Specifications for Design of Highway Steel Bridge*. China Communications Press.

Nakashima, M., Inoue, K., & Tada, M. (1998). Classification of damage to steel buildings observed in the 1995 Hyogoken-Nanbu earthquake. *Engineering Structures, 20*, 271–281.

Peng, Z., Zhao, H., Li, X., Xiong, F., & Zhu, T. (2024). New ultra-low cycle fatigue model for metal alloys. *Journal of Constructional Steel Research*, *217*, 108650. https://doi.org/10.1016/j.jcsr.2024.108650.

Rice, J. R., & Tracey, D. M. (1969). On the ductile enlargement of voids in triaxial stress fields. *Journal of the Mechanics and Physics of Solids*, *17*(3), 201–217.

Shi, Y., & Zhou, Y. (2006). *Detailed explanation of ABAQUS finite element analysis examples*. Mechanical Industry Press.

Tang, Z., Hu, X., Jiang, J., Xue, H., & Zhuge, H. (2022). Effects of pre-fatigue damages on ultimate strength of steel columns: From material to structure. *Journal of Constructional Steel Research*, *195*, 107358.

Tang, Z., Xue, H., Liu, H., & Zhang, W. (2021). Prediction of ultralow cycle fatigue damage of thin-walled steel bridge piers. *Advanced Steel Construction*, *17*(4), 403–411.

Tong, L., Huang, X., Zhou, F., & Chen, Y. (2016). Experimental and numerical investigations on extremely-low-cycle fatigue fracture behavior of steel welded joints. *Journal of Constructional Steel Research, 119*(1), 98–112.

Wang, H., Xu, S., Li, A., & Kang, K. (2018). Experimental and numerical investigation on seismic performance of corroded welded steel connections. *Engineering Structures*. https://doi.org/10.1016/j.engstruct.2018.07.057

Watanabe, E., Sugiura, K., & Oyawa, W. O. (2000). Effects of multi-directional displacement paths on the cyclic behavior of rectangular hollow steel column. *Journal of Structural Engineering and Earthquake Engineering, 17*(1), 69–85.

Wong, Y., Paulay, T., & Priestley, M. J. N. (1993). Response of circular reinforced concrete columns to multi-directional seismic attack. *Aci Structural Journal, 90*(2), 180–191.

Xie, X., Cheng, C., & Li, S. (2020). A deformation history-based approach for ultra-low cycle fatigue damage evaluation of steel structures. *International Journal of Steel Structures, 20*(4), 1378–1392.

Xie, X., Zhuge, H., Tang, Z., Wang, T., & Liao, Y. (2018). Damage characteristics of thin-walled steel arch bridges subjected to in-plane earthquake action. *Journal of Constructional Steel Research*. https://doi.org/10.1016/j.jcsr.2018.08.036

Yu, M., Xie, X., & Cheng, C. (2024). Ultra-low cycle fatigue evaluation method for unstiffened steel piers using fiber model. *Journal of Constructional Steel Research, 213*, 108373.

Zhuge, H., Xie, X., Li, S., & Wang, J. (2020). Seismic performance test and practical calculation method of thin-walled square-section steel piers under bi-directional seismic excitation. *China Civil Engineering Journal, 53*(12), 74–85. (in Chinese).